DTU Library

Decadal to Centennial Timescale Mantle Viscosity Inferred from Modern Crustal Uplift Rates in Greenland

Adhikari, S.; Milne, G. A.; Caron, L.; Khan, S. A.; Kjeldsen, K. K.; Nilsson, J.; Larour, E.; Ivins, E. R.

[Link back to DTU Orbit](#)

Decadal to Centennial Timescale Mantle Viscosity Inferred From Modern Crustal Uplift Rates in Greenland

S. Adhikari[1] , G. A. Milne[2] , L. Caron[1] , S. A. Khan[3] , K. K. Kjeldsen[4] , J. Nilsson[1] , E. Larour[1] , and E. R. Ivins[1]

[1]Jet Propulsion Laboratory, California Institute of Technology, Pasadena, CA, USA, [2]Department of Earth and Environmental Sciences, University of Ottawa, Ottawa, ON, Canada, [3]Department of Geodesy and Earth Observations, Technical University of Denmark, Kgs. Lyngby, Denmark, [4]Geological Survey of Denmark and Greenland, Copenhagen, Denmark

Abstract The observed crustal uplift rates in Greenland are caused by the combined response of the solid Earth to both ongoing and past surface mass changes. Existing elastic Earth models and Maxwell linear viscoelastic GIA (glacial isostatic adjustment) models together underpredict the observed uplift rates. These models do not capture the ongoing mantle deformation induced by significant ice melting since the Little Ice Age. Using a simple Earth model within a Bayesian framework, we show that this recent mass loss can explain the data-model misfits but only when a reduced mantle strength is considered. The inferred viscosity for sub-centennial timescale mantle deformation is roughly one order of magnitude smaller than the upper mantle viscosity inferred from GIA analysis of geological data. Reconciliation of geological sea-level and modern crustal motion data may require that the model effective viscosity be treated with greater sophistication than in the simple Maxwell rheological paradigm.

Plain Language Summary There are 57 permanent Global Navigation Satellite System (GNSS) stations on bedrock in Greenland. These stations provide point-measurements of three-dimensional crustal motion. We can model a large portion of the observed crustal uplift rates as elastic Earth response to ongoing rates of ice-mass loss. We model the remaining part of the uplift rates as the ongoing viscous response of the solid Earth to past ice-ocean mass exchange—a process termed glacial isostatic adjustment (GIA). Earth structure and deglaciation history in GIA models are usually constrained by geological data that record paleo sea level and past ice margins. To fully explain the GNSS-measured uplift rates, we propose that these geologically constrained GIA models should additionally resolve: (a) ice-mass changes during and after the Little Ice Age; and (b) broadband mantle relaxation processes. While such features are challenging to implement, they offer a more granular model paradigm appropriate to the improved temporal sampling that the collective geological and geodetic data sets now provide.

1. Introduction

There are 57 permanent Global Navigation Satellite System (GNSS) stations placed on the bedrock along the periphery of the Greenland Ice Sheet (GrIS). This network of GNSS stations—known as GNET (Bevis et al., 2012; Khan et al., 2016)—provides point measurements of 3-D bedrock motion. Some of these stations have been in operation since 1995, providing a valuable data set for probing causal relationships between ice load and solid-Earth deformation over a range of timescales. Interannual, seasonal, or shorter timescale GNET signals are interpreted as an elastic response of the solid Earth to short-period surface mass changes in Greenland, including fluctuations in mass transport through outlet glaciers and atmospheric pressure variability (e.g., Adhikari et al., 2017; Bevis et al., 2012; Zhang et al., 2019). The bedrock uplift as measured by GNET is also shown to track the apparent acceleration of ice mass change that is ongoing in Greenland (Bevis et al., 2019). Geophysical interpretation of secular trends in vertical bedrock motion—henceforth termed "uplift rates"—is ambiguous (e.g., Khan et al., 2016; Milne et al., 2018; Simpson et al., 2011; van Dam et al., 2017). We seek to reduce this ambiguity through improved quantification of the relative contributions of contemporary and past load changes to the measured uplift rates, especially those associated with the emergence of Greenland from the Little Ice Age (LIA).
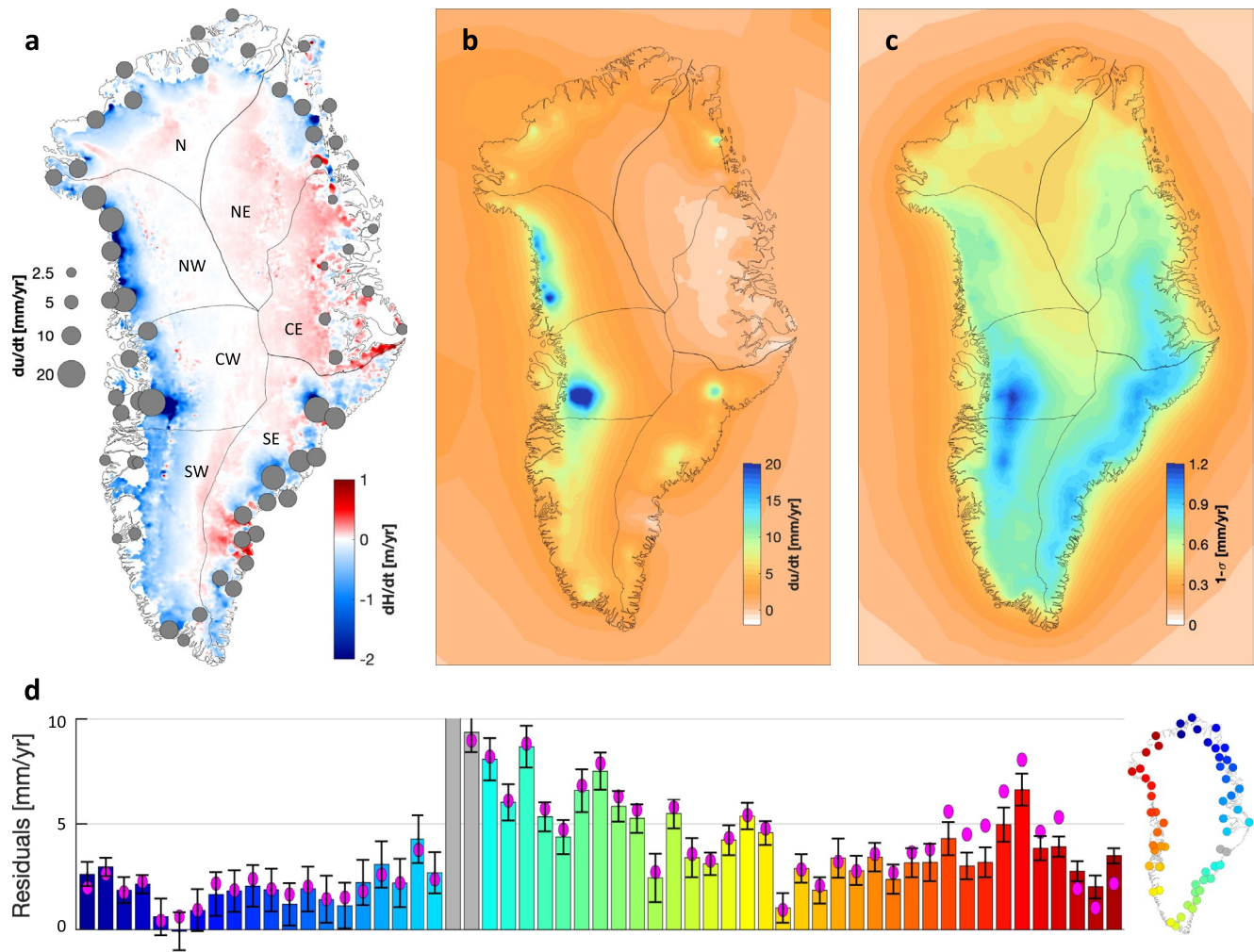
Figure 1. Observed and modeled uplift rates and the residuals. (a) The positions of 57 Global Navigation Satellite System (GNSS) stations are shown with gray circles, whose size represents the average rate of crustal uplift, du/dt, measured during 2011–2016. The background map shows the mean rate of ice thickness change, dH/dt, during the same period. Following Kjeldsen et al. (2015), we outline seven regions for which the so-called glacial isostatic adjustment (GIA) corrections are estimated for GRACE and GRACE-FO missions (Table S1). Labels refer to north (N), northeast (NE), northwest (NW), central east (CE), central west (CW), southeast (SE) and southwest (SW). (b) Mean and (c) 1-σ uncertainty of elastic uplift rates induced by present-day ice thickness change. (d) Residual uplift rates at the GNSS stations, derived by subtracting the sum of the elastic and GIA uplift rates from the measured rates. The bars are based on the GIA solutions of Milne et al. (2018), and the maroon dots are based on the solutions of Lecavalier et al. (2014). Two stations located near Kangerlussuaq Glacier (gray circles in the right-side inset), whose residuals are shown with gray bars, are excluded from further analysis because their measurements are thought to be affected by the passage of the Icelandic hotspot (Khan et al., 2016), a feature not treated here.

Figure 1a shows the uplift rates measured over 2011–2016, derived by fitting the daily GNET data with a linear trend featuring periodic seasonal signals. The measured uplift rates in Greenland is primarily driven by surface loading phenomena. Of prime importance is a climate-driven transport of ice and water mass between the continents and the ocean over a range of timescales. These include the ongoing mass loss from the GrIS and peripheral glaciers since the LIA maximum (Khan et al., 2020; Kjeldsen et al., 2015; Marzeion et al., 2015; Mouginot et al., 2019; The IMBIE Team, 2020), and the deglaciation of Greenland and nearby ice sheets during the Late Quaternary and Holocene and the associated change in relative sea-level (RSL) (e.g., Fleming & Lambeck, 2004; Lecavalier et al., 2014; Simpson et al., 2009; Tarasov et al., 2012; Tarasov & Peltier, 2002). The response of the solid Earth to these surface loads is typically modeled by considering elastic Earth deformation due to present-day surface mass changes and a delayed viscous response of the mantle induced by past load changes, a process referred to as glacial isostatic adjustment (GIA). The

existing GIA models constrained by paleo RSL data generally do not fit the uplift rates corrected for the elastic loading effects (Khan et al., 2016; Milne et al., 2018; Simpson et al., 2011; van Dam et al., 2017).

Our main goal here is to better understand this general inconsistency between the observed and modeled uplift rates in Greenland through a closer examination of the model-predicted viscoelastic Earth deformation. We determine an improved elastic contribution by incorporating the present-day surface mass changes at kilometer-scale resolution and producing uncertainty estimates of both the surface load and the elastic Earth structure. We also develop an improved GIA model by considering ice mass changes since the Medieval Warm Period (MWP) that preceded the LIA, which are either omitted or poorly represented in previous studies (e.g., Lecavalier et al., 2014; Milne et al., 2018; Peltier et al., 2015; Simpson et al., 2009; Wake et al., 2016).

2. Elastic Uplift Rates

Satellite altimetry and gravimetry measurements have provided unprecedented constraints on the spatio-temporal distribution of Greenland ice mass change over the past three decades (Mouginot et al., 2019; Sasgen et al., 2020; The IMBIE Team, 2020). CryoSat-2 measurements of surface elevation change are available at a kilometer-scale resolution. From these, we estimate that Greenland, including peripheral glaciers, has lost ice mass at an average rate of 237 ± 47 Gt/year between January 2011 and December 2016. We use the methods of Nilsson et al. (2016) to process the satellite altimetry data and apply an appropriate correction for firn air content to derive the ice-equivalent surface elevation change using the Regional Atmospheric Climate Model (RACMO) predictions (Noël et al., 2016). Figure 1a shows the spatial pattern of the rate of ice height change during 2011–2016. The modeled uplift rates at GNSS stations are sensitive to the spatial structure of the surface mass changes (Adhikari et al., 2017). It is, therefore, essential to resolve these surface changes with a high level of spatial fidelity. For improved predictions of the elastic uplift, it is also important to consider contemporary mass changes in adjacent areas, especially those occurring in the Canadian Arctic where significant amount of ice has been lost recently (Wouters et al., 2019). Here we consider the surface mass changes in the adjacent areas based on the Gravity Recovery and Climate Experiment (GRACE) data (Adhikari et al., 2019; Watkins et al., 2015). Rates of Greenland and adjacent mass changes and uncertainties therein are shown in Figure S1.

A seismologically constrained, radially stratified, 1-D Preliminary Reference Earth Model (PREM) (Dziewonski & Anderson, 1981) has been the standard model for surface loading studies, although more realistic models based on considerably denser teleseismic ray sampling are available for the upper mantle and crust. Cammarano et al. (2005), for example, utilize seismic and mineral physics constraints to deduce 99 plausible 1-D profiles for the upper mantle and transition zone from global seismic data. Similarly, Laske et al. (2013) provide a 1° × 1° gridded global shallow elastic Earth structure resolving three sediment layers and three underlying layers of crystalline crust. These models are critical to regional loading studies, as they define short-wavelength features that may influence the predicted uplift rates. The Laske et al. (2013) inferences of both density and Poisson's ratio in Greenland, averaged over the upper 50 km of solid Earth, are each smaller than corresponding values from PREM by several percent (Figure S2). We combine PREM with more recent upper mantle (Cammarano et al., 2005) and crustal (Laske et al., 2013) models to generate a total of 640 1-D elastic Earth models. The model ensemble provides a better approximation of the regional elastic and density structure than PREM does. It also captures the uncertainties that can be propagated into modeled uplift rates for Greenland. Given 1-D profiles of density and Lamé parameters, we solve a linear system of equations for the perturbations in motion and gravitation subjected to appropriate boundary conditions in order to calculate the so-called load Love numbers (Longman, 1962). We define corresponding Green's functions (Farrell, 1972) that can be convolved with surface loads to calculate the elastic bedrock motion (Adhikari et al., 2017). We perform benchmark experiments for PREM and compare them to our regionally adapted elastic Earth models, both in terms of Love numbers and the modeled uplift rates (Figure S2).

Our estimates of both the elastic uplift rates and uncertainties are shown in Figures 1b and 1c. On average, the Greenland crust experienced uplift during 2011–2016. The central east region, however, subsided at a small rate of ~1 mm/year. The highest uplift rates are found along the ice margin and in the ablation zone and generally decrease toward both the ocean and inland, reflecting the spatial pattern of the measured

ice thinning rates (Figure 1a). Mass changes in the adjacent regions contribute to uplift at a peak rate of ~1 mm/year in the northwest but are generally negligible elsewhere in Greenland (Figure S3). Our uncertainty estimate combines those associated with both the surface load and elastic Earth structure. For ice thickness change, both measurement and instrument uncertainties are quantified (Nilsson et al., 2016), as well as those associated with the model-based estimate of firn air content (Noël et al., 2016). The uncertainty in mass change in the adjacent areas is taken from Adhikari et al. (2019). We find that the solid Earth model uncertainty is generally smaller than the absolute bias in the modeled uplift rates relative to PREM and that the surface load, rather than the elastic Earth structure, is the dominant source of uncertainty in the modeled uplift rates (Figure S3).

3. GIA and Residual Uplift Rates

Model reconstructions of Greenland and nearby ice sheets during the late Quaternary and Holocene are constrained by a suite of geological and geodetic data sets (e.g., Fleming & Lambeck, 2004; Lecavalier et al., 2014; Tarasov et al., 2012; Tarasov & Peltier, 2002). These reconstructions are often limited in spatial and temporal resolution, although high spatiotemporal reconstructions are becoming available at least for part of Greenland (Briner et al., 2020; Cuzzone et al., 2019). Of particular relevance to this study is that surface load changes on decadal to century timescales are not well captured in GIA models. Previous GIA modeling studies have generally utilized available RSL data in order to constrain solid Earth properties, especially the 1-D radial profile of mantle viscosity (e.g., Caron et al., 2018; Lambeck et al., 2014, 2017; Lau et al., 2016). While regional geophysical data reveal significant lateral variability in Earth structure beneath Greenland (Darbyshire et al., 2018; Pourpoint et al., 2018; Steffen et al., 2018), to our knowledge, no GIA studies have yet incorporated these constraints in 3-D Earth models. Milne et al. (2018) determined a small number of plausible 3-D Earth structures using constraints from global models of seismic velocity (Auer et al., 2014; French & Romanowicz, 2014; Ritsema et al., 2011; Schaeffer & Lebedev, 2013) and lithosphere thickness (Zhong et al., 2003; Conrad & Lithgow-Bertelloni, 2006) and investigated the impact of 3-D Earth structures on the modeled deglacial RSL changes and modern crustal uplift rates. The deglacial load model and the laterally averaged Earth structure considered by Milne et al. (2018) are the same as those constrained using geological records of ice extent and RSL (Lecavalier et al., 2014).

The modeled uplift rates and associated uncertainties from Milne et al. (2018) are shown in Figure S4. These solutions account for part of the uncertainty associated with the lateral Earth structure and do not account for that associated with the deglaciation history. Large subsidence is predicted in southwest Greenland owing to the mid to late Holocene ice-sheet readvance and the forebulge collapse associated with the North American ice sheets (Lecavalier et al., 2014 and references therein), while considerable uplift is predicted in the north. This pattern is also evident in 1-D model solutions (e.g., Simpson et al., 2011; The IMBIE Team, 2020; Wake et al., 2016), implying that GIA models for Greenland constrained by geological data sets are in broad agreement, at least, in terms of the spatial pattern of modeled uplift rates. We combine the model output of Milne et al. (2018) with the improved elastic uplift rates (Section 2) and find large disagreement with the observed rates at virtually all GNET stations (Figure 1d). The average data-model misfit is 3.4 ± 1.9 mm/year, with relatively larger misfits in the central west and southeast Greenland. These residuals, which have also been reported in previous studies (Khan et al., 2016; Milne et al., 2018; Simpson et al., 2011; van Dam et al., 2017), are much larger than the observational uncertainty at most sites and therefore require an additional geophysical explanation. Following Simpson et al. (2011), we hypothesize that the ongoing solid Earth response to the post-MWP load changes, especially the post-LIA mass loss, explains the residual uplift rates (Figure 1d). Despite the significant amount of mass being lost from Greenland over the past ~150 years (Khan et al., 2020; Kjeldsen et al., 2015; Marzeion et al., 2015), this recent deglaciation sequence is generally not accurately accounted for in ice sheet reconstructions tuned to geological RSL observations.
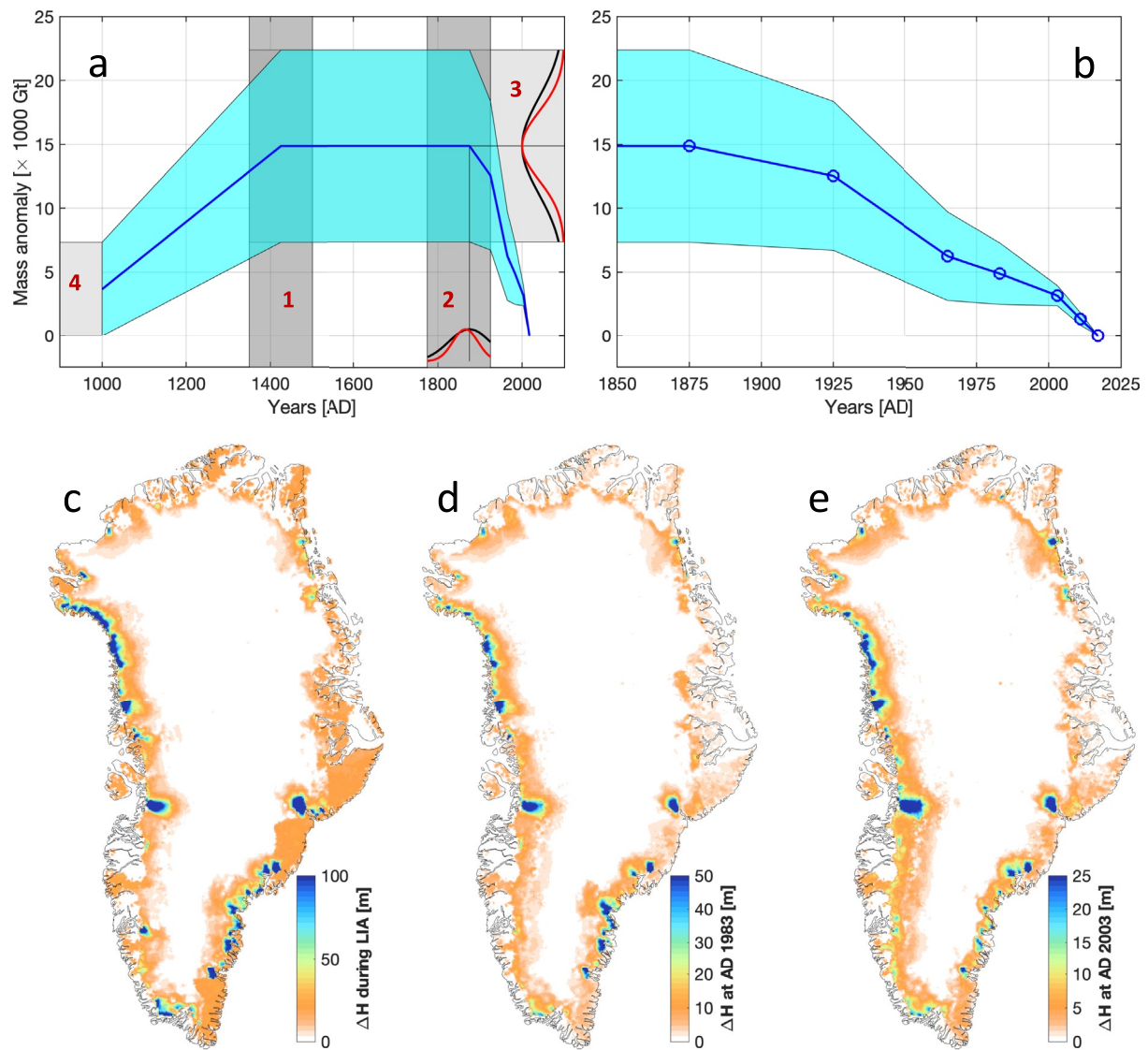
Figure 2. Post-Medieval Warm Period (MWP) loading history considered in our Bayesian exploration. (a) Summary of ice load history and uncertainty therein. Free parameters 1 and 2 (shown with vertical shadows) determine the inception and termination timing of the Little Ice Age (LIA), respectively, and parameters 3 and 4 (horizontal shadows) are related to the amplitude of the mass anomaly during the LIA and MWP, respectively. A priori likelihood is imposed for parameters 2 and 3; black and red Gaussian functions show, respectively, the prior and (normalized) posterior probabilities. (b) A zoom-in of the loading history over the past 170 years. (c–e) Spatial distribution of ice thickness anomaly, relative to AD 2016, at select times: during the LIA maximum, at AD 1983 and 2003, respectively.

4. Post-MWP Loading and Solid Earth Response

Kjeldsen et al. (2015) provide a reconstruction of the post-LIA mass balance of the GrIS by investigating digital elevation models based on aerial imagery and historical maps with remarkable detail along much of the ice sheet periphery. They also utilize modern geodetic measurements of airborne and satellite altimetry to estimate ice sheet mass balance during the periods 1983–2003 and 2003–2010. The historical mass balance of Greenland peripheral glaciers has been modeled based on reconstructed climate data and found to be consistent with observations of glacier mass balance and ice volume change (Marzeion et al., 2015). This reconstruction reveals that more than three-quarters of total glacier mass loss since the LIA occurred during 1925–1965 (Figure S5). We combine the ice sheet and peripheral glacier data to construct a time series of the post-LIA ice thickness anomaly, relative to AD 2016, assuming linear changes in thickness over the periods: LIA-1925, 1925–1965, 1965–1983, 1983–2003, 2003–2011, and 2011–2016 (Figure 2). As the spatial pattern

of glacier mass evolution is not available, we distribute the mass anomaly (Marzeion et al., 2015) uniformly over the present-day glacier surface area as defined in the Randolph Glacier Inventory version 5.0 (Pfeffer et al., 2014). To encompass the entirety of the LIA period in our load model, we extend the loading history back to the preceding MWP (to be discussed later) whose median year is assumed to be AD 1000 (Figure 2a).

We explore the contribution of this recent loading sequence to present-day uplift rates with the aim of explaining the relatively large data-model misfits in question. GIA modeling approaches generally tune the viscosity structure of the mantle in order to fit geological data sets, especially the globally distributed paleo-RSL data that span the past ~20,000 years. In Greenland, inferred values for the upper mantle viscosity are on the order of 5×10^{20} Pa s (Fleming & Lambeck, 2004; Lecavalier et al., 2014; Simpson et al., 2009). For this value of mantle viscosity, the post-MWP mass changes (Figure 2) yield present-day uplift rates at the sub-millimeter per year level (Figure S6). We have also explored the influence of lateral variations in lithospheric thickness and sub-lithosphere viscosity structure using a subset of the models considered by Milne et al. (2018). Specifically, we generated results based on the seismic models S40RTS (Ritsema et al., 2011) and SL2013sv (Schaeffer & Lebedev, 2013) and the lithospheric thickness model of Zhong et al. (2003). We find that the impact of these lateral heterogeneity models on the predicted post-MWP signal is generally insignificantly different, except for a few stations in the central east where the effect of the Icelandic hot plume is well documented (Figure S7). We conclude that including a geologically-constrained viscosity structure, with or without lateral heterogeneity, does not result in uplift rates associated with the post-MWP loading that are large enough to explain the data-model misfits.

We therefore postulate the importance of alternative mantle relaxation processes that are either governed by inherently transient rheology (Ivins et al., 2020; Lau et al., 2020) or by non-linear stress-dependent rheology (Blank et al., 2021). Such enhancement of the relaxation process acts to lower the effective viscosity on timescales of decades to centuries and thus produce more rapid uplift rates for post-MWP mass changes. To a first approximation, the possibility of reduced mantle strength can be tested using any Maxwell model (e.g., Barletta et al., 2018; Nield et al., 2014). Here we consider an incompressible half-space Earth deformation model with an elastic lithosphere over a Maxwell mantle rheology (Adhikari et al., 2014; Ivins & James, 1999), which places an upper bound on the effective viscosity reduction required to reconcile RSL and GNSS data sets (to be discussed later). As we explore model parameter tradeoffs within the formal Bayesian framework, the consideration of more comprehensive Earth models (both in terms of rheology and spatial structure) is not feasible due to the associated computational burden. Here, we independently vary a total of six parameters within their respective plausible ranges: lithosphere thickness, mantle viscosity, and four parameters related to the deglaciation history (Figure 2a). The latter set of parameters include (a) LIA inception time; (b) LIA termination time; (c) amplitude of the mass anomaly during LIA; and (d) amplitude of the mass anomaly during the MWP.

The duration and timing of the LIA can vary considerably from glacier to glacier, even within the same fjord system. For example, in Nuuk fjord in southwest Greenland, the marine-terminating Kangiata Nunaata Sermia was at its LIA maximum extent at 1761 and had already retreated ~5 km by 1808 (Lea et al., 2014), while the nearby Narsap Sermia remained close to its LIA maximum extent until as late as the early 2000s (Motyka et al., 2017). Due to a lack of such a comprehensive record for many glaciers, it is not feasible to consider glacier-specific timings of the LIA. Several lines of evidence based on geological, archeological, lake sediment, and ice core studies suggest that most of the Greenland glaciers advanced to their maximum extents sometime in the period 1400–1900 (e.g., Fischer et al., 1998; Grove, 1988; Kelly & Lowell, 2009; Larsen et al., 2015; Woodroffe et al., 2017). While the LIA inception time is relatively uncertain, which we consider here to vary between 1350 and 1500, the termination time is generally better constrained through a combination of above-noted data sets. In various sectors of Greenland, glaciers began a retreat from their respective maximum extents at various times, roughly centered around 1850–1900. For example, Jakobshavn Isbræ in the central west began to retreat from its maximum extent before 1850 (Briner et al., 2011; Khan et al., 2015), while Helheim and Kangerdlugssuaq glaciers in the southeast began to retreat since ~1930 (Khan et al., 2014). We consider this parameter (i.e., termination time) to vary with a Gaussian prior centered at AD 1875 having a standard deviation of 50 years. Due to modern geodetic measurements and modeling capabilities, the ice thickness change since 1983 has been quantified with relatively little ambiguity. The ice thickness anomaly during the LIA has relatively large uncertainty. A total of 14,862 ± 3,758 Gt

of LIA mass anomaly is estimated for the GrIS and peripheral glaciers (Kjeldsen et al., 2015; Marzeion et al., 2015). We consider this parameter to vary with a Gaussian prior estimate. We assume that the ice thickness, and by inference the mass, does not evolve during the LIA. Finally, we bound the MWP ice mass to be no less than the present-day value and no more than that during the LIA (Figure 2a).

We simulate an ensemble of 3,000 1-D viscoelastic Earth model simulations. Each model considers a unique ice load history and solid Earth parameters sampled by a simulated annealing algorithm (Caron et al., 2018). Based on the predicted uplift rates, we construct a misfit function for each model as follows

$$J_i = \frac{m_i - d_i}{\sigma_i},$$ (1)

where m_i and d_i are the model prediction and the target value (i.e., the residual uplift rate) at the -th GNSS station, respectively, and σ_i is the associated data uncertainty. We have a total of $N_{data} = 55$ constraining data points (Figure 1d). We construct the model likelihood function, L, as follows

$$L = \exp\left(-\frac{1}{2N_{data}} \sum_{i=1}^{N_{data}} J_i^2\right),$$ (2)

which represents the likelihood of a given model to explain the target uplift rates and, hence, serves as a weighting factor in our statistics of the model parameters and the predicted uplift rates. Given a multivariate Gaussian prior, the posterior probability, p, that updates our prior state of knowledge with information gained during the inversion (i.e., the likelihood function) is given by

$$p \propto L \exp\left(-\frac{1}{2}(\mathbf{x} - \boldsymbol{\mu})\mathbf{E}^{-1}(\mathbf{x} - \boldsymbol{\mu})^{\mathrm{T}}\right).$$ (3)

Here $\mathbf{x}$ is the row vector of parameter values that have Gaussian priors (see Figure 2a), $\boldsymbol{\mu}$ is the corresponding vector of prescribed parameter means, and $\mathbf{E}$ is the covariance matrix. We assume these parameters to be independent of one another, or, in other words, with correlation coefficients equal to zero.

Posterior probability density functions (PDFs) projected into 2-D spaces formed by each pair of parameters are shown in Figure S8. We find that our solutions are insensitive to two of the most uncertain parameters: the MWP ice mass anomaly and the LIA inception time. The solution is relatively weakly dependent on the lithosphere thickness, although it has a slight trade-off with mantle viscosity. Posterior statistics of the LIA mass anomaly ($14,860 \pm 2,670$ Gt) and the termination time (AD 1865 ± 30) are not much different from those of the prior PDFs in terms of their means, although they exhibit reduced variance in both cases. One feature that stands out in the posterior PDFs is the correlation between the LIA mass anomaly and the mantle viscosity. Models with larger LIA mass anomaly perform better when the mantle viscosity is also larger. Given our knowledge of the LIA mass anomaly and its uncertainty (Kjeldsen et al., 2015; Marzeion et al., 2015), we find the preferred mantle viscosity to be in the range of $6 - 11 \times 10^{19}$ Pa s, which is smaller than the local upper mantle viscosity inferred in Greenland GIA studies by a factor of 4–8 (Fleming & Lambeck, 2004; Lecavalier et al., 2014; Simpson et al., 2009). Had our Earth structure model included increases in viscosity with depth, our preferred values for the asthenospheric environment would be even lower. Indeed, a 3-layer spherical Earth model featuring a 120-km thick lithosphere and 2×10^{21} Pa s lower mantle viscosity (Lecavalier et al., 2014) yields the upper mantle viscosity value of 3×10^{19} Pa s (Figure S9).

5. Improved GIA Uplift Rates

Figures 3a and 3b show the expected uplift rates and associated uncertainties that are attributable to the post-MWP load changes. Large uplift rates of order 3–5 mm/year are predicted along the coastal margins in the west and southeast. While at many GNET stations our predictions are within 1-σ uncertainties of target values, there are a few stations where we fail to predict the uplift rates even within 3-σ uncertainties (Figure S10). Our attempt to vary regional deglaciation history independently (see Figure 1a for the regional outline) does not reduce the misfit. A more granular deglaciation history than is presented here might be possible as the constraining data are improved (e.g., Briner et al., 2020). Furthermore, we have hardly exhausted the full list of additional complexities to invoke in the underlying constitutive approximations governing the deforming solid Earth (e.g., Blank et al., 2021; Ivins et al., 2020; Lau & Holtzman, 2019). One result, nevertheless, is inescapable: incorporation of the post-MWP load model coupled to an upper mantle
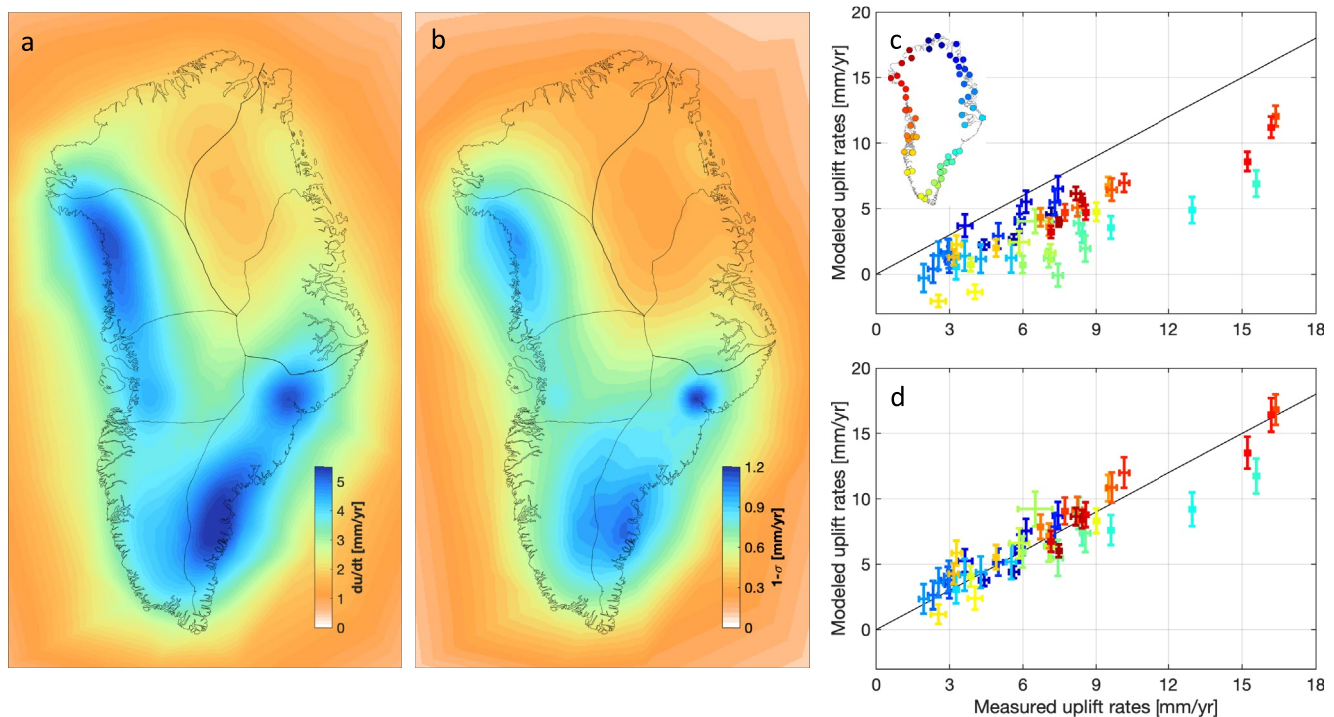
Figure 3. Crustal uplift rates due to the post-Medieval Warm Period (MWP) loading and improvements to Global Navigation Satellite System (GNSS) data fit. (a) Expected uplift rates due to the post-MWP loading history and (b) associated uncertainties inferred from our Bayesian analysis. (c) The summed elastic (Section 2) and glacial isostatic adjustment uplift rates (Section 3) plotted against the measured GNSS uplift rates at 55 GNET stations. (d) Same as c but after adding the post-MWP load induced uplift rates to the modeled rates. Notice the improvement to data fit and an overall reduction in data variance.

of reduced creep strength compared to values found in previous GIA studies substantially improves the overall GNSS data fit (compare Figure 3c vs. Figure 3d).

Our uplift rates associated with the post-MWP loading (Figures 3a–3b) are combined with the deglacial uplift rates (Figure S4) to give a comprehensive picture of the ongoing (viscous) solid Earth deformation induced by past load changes (Figure S11). The combined uplift rate—termed "improved" GIA uplift rate—at the KULU station in southeast Greenland is 4.71 ± 0.93 mm/year, which is consistent with the estimate of van Dam et al. (2017) who deduce the corresponding uplift rate to be 4.49 ± 1.44 mm/year from GNSS and absolute gravity data. The agreement is important as the data combination method used by van Dam et al. (2017) uniquely isolates the relative contributions of contemporary (elastic) and past (viscous) load changes to the GNSS rate.

The improved GIA uplift rates have ramifications for reinterpreting ice-sheet mass balance from space gravimetry. For example, a recent reanalysis of the first three years of the GRACE mission data (2002–2005) determined mass balance during that period at roughly -180 Gt/year (Velicogna et al., 2020). The improved GIA correction developed here increases that estimate by more than 10% to near -200 Gt/year (Table S1). The increase is due to the more robust GIA-related positive trend in geoid change—primarily owing to the post-LIA ice mass loss and associated sub-centennial timescale mantle deformation—and is consistent with the estimates of Khan et al. (2016) and Sasgen et al. (2020) who provide direct GNSS constraints to their respective GIA models.

6. Conclusions

Previous efforts to explain the modern crustal uplift rates in Greenland have considered the elastic response of solid Earth to contemporary surface mass changes and the viscous deformation of mantle induced by deglaciation of Greenland and nearby ice sheets during the Late Pleistocene and Holocene (Khan et al., 2016; Milne et al., 2018). What has been missing in these studies is the consideration of the ongoing solid Earth

response to more recent mass loss following the Little Ice Age (Kjeldsen et al., 2015; Simpson et al., 2011). Here we show that the consideration of this recent loading history results in uplift rates that are sufficient to explain the majority of data-model misfits but only when a relatively reduced mantle strength is considered. The viscosity for sub-centennial timescale mantle deformation resolved by our constraining data is roughly one order of magnitude smaller than the upper mantle viscosity typically inferred in GIA analysis of relative sea-level data. Future glacial loading studies should, therefore, consider a more comprehensive than the Maxwell mantle rheological model that captures mantle relaxation across a range of timescales (Blank et al., 2021; Caron et al., 2017; Ivins et al., 2020; Lau et al., 2020; Lau & Holtzman, 2019). Laboratory experiments of rock creep at high temperature and pressure environments (e.g., Faul & Jackson, 2015; Kohlstedt & Hansen, 2015) and recent studies of post-seismic mantle flow (e.g., Liu et al., 2020; Muto et al., 2019; Pollitz, 2019) suggest the necessity of considering such higher-order constitutive relations.

Data Availability Statement

The authors use an open-source software package Ice-sheet and Sea-level System Model (ISSM; https://issm.jpl.nasa.gov/) to compute the elastic and post-MWP uplift rates. Earth models, associated Love numbers, and modeled uplift rates are stored and visualized at JPL's Virtual Earth System Laboratory (https://vesl.jpl.nasa.gov/visualizations/solid-earth/greenland-crustal-motion/).

References

Adhikari, S., Ivins, E. R., Frederikse, T., Landerer, F. W., & Caron, L. (2019). Sea-level fingerprints emergent from GRACE mission data. *Earth System Science Data*, *11*, 629–646. https://doi.org/10.5194/essd-11-629-2019

Adhikari, S., Ivins, E. R., & Larour, E. (2017). Mass transport waves amplified by intense Greenland melt and detected in solid Earth deformation. *Geophysical Research Letters*, *44*, 4965–4975. https://doi.org/10.1002/2017gl073478

Adhikari, S., Ivins, E. R., Larour, E., Seroussi, H., Morlighem, M., & Nowicki, S. (2014). Future Antarctic bed topography and its implications for ice sheet dynamics. *Solid Earth*, *5*, 569–584. https://doi.org/10.5194/se-5-569-2014

Auer, L., Boschi, L., Becker, T. W., Nissen-Meyer, T., & Giardini, D. (2014). Savani: A variable resolution whole-mantle model of anisotropic shear velocity variations based on multiple data sets. *Journal of Geophysical Research*, *119*, 3006–3034. https://doi.org/10.1002/2013jb010773

Barletta, V., Bevis, M., Smith, B. E., Wilson, T., Brown, A., Bordoni, A., et al. (2018). Observed rapid bedrock uplift in Amundsen Sea Embayment promotes ice-sheet stability. *Science*, *360*(6395), 1335–1339. https://doi.org/10.1126/science.aao1447

Bevis, M., Harig, C., Khan, S. A., Brown, A., Simons, F. J., Willis, M., et al. (2019). Accelerating changes in ice mass within Greenland, and the ice sheet's sensitivity to atmospheric forcing. *Proceedings of the National Academy of Sciences*, *116*(6), 1934–1939. https://doi.org/10.1073/pnas.1806562116

Bevis, M., Wahr, J., Khan, S. A., Madsen, F. B., Brown, A., Willis, M., et al. (2012). Bedrock displacements in Greenland manifest ice mass variations, climate cycles and climate change. *Proceedings of the National Academy of Sciences*, *109*, 11944–11948. https://doi.org/10.1073/pnas.1204664109

Blank, B., Barletta, V., Hu, H., Pappa, F., & van der Wal, W. (2021). Effect of lateral and stress-dependent viscosity variations on GIA induced uplift rates in the Amundsen Sea Embayment. *Geochemistry, Geophysics, Geosystems*. *22*(9), e2021GC009807. https://doi.org/10.1029/2021GC009807

Briner, J., Cuzzone, J. K., Badgeley, J. A., Young, N. E., Steig, E. J., Morlighem, M., et al. (2020). Rate of mass loss from the Greenland Ice Sheet will exceed Holocene values this century. *Nature*, *586*, 70–74. https://doi.org/10.1038/s41586-020-2742-6

Briner, J., Young, N. E., Thomas, E. K., Stewart, H. A. M., Losee, S., & Truex, S. (2011). Varve and radiocarbon dating support the rapid advance of Jakobshavn Isbrae dring the Little Ice Age. *Quaternary Science Reviews*, *30*(19–20), 2476–2486. https://doi.org/10.1016/j.quascirev.2011.05.017

Cammarano, F., Deuss, A., Goes, S., & Giardini, D. (2005). One-dimensional physical reference models for the upper mantle and transition zone: Combining seismic and mineral physics constraints. *Journal of Geophysical Research*, *110*, B01306. https://doi.org/10.1029/2004jb003272

Caron, L., Ivins, E. R., Larour, E., Adhikari, S., Nilsson, J., & Blewitt, G. (2018). GIA model statistics for GRACE hydrology, cryosphere, and ocean science. *Geophysical Research Letters*, *45*, 2203–2212. https://doi.org/10.1002/2017gl076644

Caron, L., Métivier, L., Greff-Lefftz, M., Fleitout, L., & Rouby, H. (2017). Inverting glacial isostatic adjustment signal using Bayesian framework and two linearly relaxing rheologies. *Geophysical Journal International*, *209*, 1126–1147. https://doi.org/10.1093/gji/ggx083

Conrad, C., & Lithgow-Bertelloni, C. (2006). Influence of continental roots and asthenosphere on plate-mantle coupling. *Geophysical Research Letters*, *33*, L05312. https://doi.org/10.1029/2005gl025621

Cuzzone, J., Schlegel, N.-J., Morlighem, M., Larour, E., Briner, J. P., Seroussi, H., & Caron, L. (2019). The impact of model resolution on the simulated Holocene retreat of the southwestern Greenland ice sheet using the Ice Sheet System Model (ISSM). *The Cryosphere*, *13*, 879–893. https://doi.org/10.5194/tc-13-879-2019

Darbyshire, F., Dahl-Jensen, T., Larsen, T. B., Voss, P. H., & Joyal, G. (2018). Crust and uppermost-mantle structure of Greenland and the Northwest Atlantic from Rayleigh wave group velocity tomography. *Geophysical Journal International*, *212*, 1546–1569. https://doi.org/10.1093/gji/ggx479

Dziewonski, A., & Anderson, D. (1981). Preliminary reference Earth model. *Physics of the Earth and Planetary Interiors*, *25*, 297–356. https://doi.org/10.1016/0031-9201(81)90046-7

Farrell, W. (1972). Deformation of the Earth by surface loads. *Review of Geophysics*, *10*(3), 761–797. https://doi.org/10.1029/rg010i003p00761

Faul, U., & Jackson, I. (2015). Transient creep and strain energy dissipation: An experimental perspective. *Annual Review of Earth and Planetary Sciences*, *43*, 541–569. https://doi.org/10.1146/annurev-earth-060313-054732

Fischer, H., Werner, M., Wagenbach, D., Schwager, M., Thorsteinnson, T., Wilhelms, F., et al. (1998). Little ice age clearly recorded in northern Greenland ice cores. *Geophysical Research Letters*, *25*(10), 1749–1752. https://doi.org/10.1029/98gl01177

Fleming, K., & Lambeck, K. (2004). Constraints on the Greenland Ice Sheet since the Last Glacial Maximum from sea-level observations and glacial-rebound models. *Quaternary Science Reviews*, *23*, 1053–1077. https://doi.org/10.1016/j.quascirev.2003.11.001

French, S., & Romanowicz, B. (2014). Whole-mantle radially anisotropic shear-velocity structure from spectral-element waveform tomography. *Geophysical Journal International*, *199*, 1303–1327. https://doi.org/10.1093/gji/ggu334

Grove, J. (1988). *The little ice age* (p. 498). London: Routledge.

Ivins, E., Caron, L., Adhikari, S., Larour, E., & Scheinert, M. (2020). A linear viscoelasticity for decadal to centennial time scale mantle deformation. *Reports on Progress in Physics*, *83*, 106801. https://doi.org/10.1088/1361-6633/aba346

Ivins, E., & James, T. (1999). Simple models for late Holocene and present-day Patagonian glacier fluctuations and predictions of a geodetically detectable isostatic response. *Geophysical Journal International*, *138*, 601–624. https://doi.org/10.1046/j.1365-246x.1999.00899.x

Kelly, M., & Lowell, T. (2009). Fluctuations of local glaciers in Greenland during latest Pleistocene and Holocene time. *Quaternary Science Reviews*, *28*(21–22), 2088–2106. https://doi.org/10.1016/j.quascirev.2008.12.008

Khan, S., Aschwanden, A., Bjørk, A. A., Wahr, J., Kjeldsen, K. K., & Kjær, K. H. (2015). Greenland ice sheet mass balance: A review. *Reports on Progress in Physics*, *78*(4), 046801. https://doi.org/10.1088/0034-4885/78/4/046801

Khan, S., Bjørk, A. A., Bamber, J. L., Morlighem, M., Bevis, M., Kjær, K. H., et al. (2020). Centennial response of Greenland's three largest outlet glaciers. *Nature Communications*, *11*, 5718. https://doi.org/10.1038/s41467-020-19580-5

Khan, S., Kjeldsen, K. K., Kjær, K. H., Bevan, S., Luckman, A., Aschwanden, A., et al. (2014). Glacier dynamics at Helheim and Kangerdlugssuaq glaciers, southeast Greenland, since the Little Ice Age. *The Cryosphere*, *8*, 1497–1507. https://doi.org/10.5194/tc-8-1497-2014

Khan, S., Sasgen, I., Bevis, M., van Dam, T., Bamber, J. L., Wahr, J., et al. (2016). Geodetic measurements reveal similarities between post-last glacial maximum and present-day mass loss from the Greenland Ice Sheet. *Science Advances*, *2*(9), e1600931. https://doi.org/10.1126/sciadv.1600931

Kjeldsen, K., Korsgaard, N. J., Bjørk, A. A., Khan, S. A., Box, J. E., Funder, S., et al. (2015). Spatial and temporal distribution of mass loss from the Greenland Ice Sheet since AD 1900. *Nature*, *528*, 396–400. https://doi.org/10.1038/nature16183

Kohlstedt, D., & Hansen, L. (2015). Constitutive equations, rheological behavior, and viscosity of rocks. In G. Schubert (Ed.), *Treatises of geophysics* (2nd ed., Vol. 2, pp. 441–472). Oxford: Elsevier. https://doi.org/10.1016/b978-0-444-53802-4.00042-7

Lambeck, K., Purcell, A., & Zhao, S. (2017). The North American Late Wisconsin ice sheet and mantle viscosity from glacial rebound analyses. *Quaternary Science Reviews*, *158*, 172–210. https://doi.org/10.1016/j.quascirev.2016.11.033

Lambeck, K., Rouby, H., Purcell, A., Sun, Y., & Sambridge, M. (2014). Sea level and global ice volumes from the Last Glacial Maximum to the Holocene. *Proceedings of the National Academy of Sciences*, *111*(43), 15296–15303. https://doi.org/10.1073/pnas.1411762111

Larsen, N., Kjær, K. H., Lecavalier, B., Bjørk, A. A., Colding, S., Huybrechts, P., et al. (2015). The response of the southern Greenland ice sheet to the Holocene thermal maximum. *Geology*, *43*(4), 291–294. https://doi.org/10.1130/g36476.1

Laske, G., Masters, G., Ma, Z., & Pasyanos, M. (2013). *Update on CRUST1.0—A 1-degree global model of Earth's crust*. EGU General Assembly. Abstract ID EGU2013-2658.

Lau, H., & Holtzman, B. (2019). "Measures of dissipation in viscoelastic media" extended: Toward continuous characterization across very broad geophysical time scales. *Geophysical Research Letters*, *46*, 9544–9553. https://doi.org/10.1029/2019gl083529

Lau, H., Holtzman, B. K., & Havlin, C. (2020). Toward a self-consistent characterization of lithospheric plates using full-spectrum viscoelasticity. *AGU Advances*, *1*, e2020AV000205. https://doi.org/10.1029/2020av000205

Lau, H., Mitrovica, J. X., Austermann, J., Crawford, O., Al-Attar, D., & Latychev, K. (2016). Inferences of mantle viscosity based on ice age data sets: Radial structure. *Journal of Geophysical Research: Solid Earth*, *121*, 6991–7012. https://doi.org/10.1002/2016jb013043

Lea, J., Mair, D. W., Nick, F. M., Rea, B. R., Weidick, A., Kjaer, K. H., et al. (2014). Terminus-driven retreat of a major southwest Greenland tidewater glacier during the early 19th century: Insights from glacier reconstructions and numerical modeling. *Journal of Glaciology*, *60*(220), 333–344. https://doi.org/10.3189/2014jog13j163

Lecavalier, B., Milne, G. A., Simpson, M. J., Wake, L., Huybrechts, P., Tarasov, L., et al. (2014). A model of Greenland ice sheet deglaciation constrained by observations of relative sea level and ice extent. *Quaternary Science Reviews*, *102*, 54–84. https://doi.org/10.1016/j.quascirev.2014.07.018

Liu, S., Shen, Z.-K., Bürgmann, R., & Jónsson, S. (2020). Thin crème brûlée rheological structure for the Eastern California Shear Zone. *Geology*, *46*, 216–221. https://doi.org/10.1130/G47729.1

Longman, I. (1962). A Green's function for determining the deformation of the Earth under surface mass loads: 1. Theory. *Journal of Geophysical Research*, *67*, 845–850. https://doi.org/10.1029/jz067i002p00845

Marzeion, B., Leclercq, P. W., Cogley, J. G., & Jarosch, A. H. (2015). Brief Communication: Global reconstructions of glacier mass change during the 20th century are consistent. *The Cryosphere*, *9*, 2399–2404. https://doi.org/10.5194/tc-9-2399-2015

Milne, G., Latychev, K., Schaeffer, A., Crowley, J. W., Lecavalier, B. S., & Audette, A. (2018). The influence of lateral Earth structure on glacial isostatic adjustment in Greenland. *Geophysical Journal International*, *214*(2), 1252–1266. https://doi.org/10.1093/gji/ggy189

Motyka, R., Cassotto, R., Truffer, M., Kjeldsen, K. K., Van As, D., Korsgaard, N. J., et al. (2017). Asynchronous behavior of outlet glaciers feeding Godthåbsfjord (Nuup Kangerlua) and the triggering of Narsap Sermia's retreat in SW Greenland. *Journal of Glaciology*, *63*(238), 288–308. https://doi.org/10.1017/jog.2016.138

Mouginot, J., Rignot, E., Bjørk, A. A., Van den Broeke, M., Millan, R., Morlighem, M., et al. (2019). Forty-six years of Greenland Ice Sheet mass balance from 1972 to 2018. *Proceedings of the National Academy of Sciences*, *116*(19), 9239–9244. https://doi.org/10.1073/pnas.1904242116

Muto, J., Moore, J. D. P., Barbot, S., Iinuma, T., Ohta, Y., & Iwamori, H. (2019). Coupled afterslip and transient mantle flow after the 2011 Tohoku earthquake. *Science Advances*, *5*(9), eaaw1164. https://doi.org/10.1126/sciadv.aaw1164

Nield, G., Barletta, V. R., Bordoni, A., King, M. A., Whitehouse, P. L., Clarke, P. J., et al. (2014). Rapid bedrock uplift in the Antarctic Peninsula explained by viscoelastic response to recent ice unloading. *Earth and Planetary Science Letters*, *397*, 32–41. https://doi.org/10.1016/j.epsl.2014.04.019

Nilsson, J., Gardner, A., Sandberg Sørensen, L., & Forsberg, R. (2016). Improved retrieval of land ice topography from CryoSat-2 data and its impact for volume-change estimation of the Greenland Ice Sheet. *The Cryosphere*, *10*, 2953–2969. https://doi.org/10.5194/tc-10-2953-2016

Noël, B., van de Berg, W. J., Machguth, H., Lhermitte, S., Howat, I., Fettweis, X., & van den Broeke, M. R. (2016). A daily, 1 km resolution data set of downscaled Greenland ice sheet surface mass balance (1958–2015). *The Cryosphere*, *10*, 2361–2377. https://doi.org/10.5194/tc-10-2361-2016

Peltier, W., Argus, D. F., & Drummond, R. (2015). Space geodesy constrains ice age terminal deglaciation: The global ICE6G_C (VM5a) model. *Journal of Geophysical Research: Solid Earth*, *120*, 450–487. https://doi.org/10.1002/2014jb011176

Pfeffer, W., Arendt, A. A., Bliss, A., Bolch, T., Cogley, J. G., Gardner, A. S., et al. (2014). The Randolph Glacier Inventory: A globally complete inventory of glaciers. *Journal of Glaciology*, *60*(221), 537–552. https://doi.org/10.3189/2014jog13j176

Pollitz, F. (2019). Lithosphere and shallow asthenosphere rheology from observations of post-earthquake relaxation. *Physics of the Earth and Planetary Interiors*, *293*, 106271. https://doi.org/10.1016/j.pepi.2019.106271

Pourpoint, M., Anandakrishnan, S., Ammon, C. J., & Alley, R. B. (2018). Lithosphere structure of Greenland from ambient noise and earthquake surface wave tomography. *Journal of Geophysical Research: Solid Earth*, *123*, 7850–7876. https://doi.org/10.1029/2018jb015490

Ritsema, J., Deuss, A. A., Van Heijst, H. J., & Woodhouse, J. H. (2011). S40RTS: A degree-40 shear-velocity model for the mantle from new Rayleigh wave dispersion, teleseismic travel time and normal-mode splitting function measurements. *Geophysical Journal International*, *184*(3), 1223–1236. https://doi.org/10.1111/j.1365-246x.2010.04884.x

Sasgen, I., Wouters, B., Gardner, A. S., King, M. D., Tedesco, M., Landerer, F. W., et al. (2020). Return to rapid ice loss in Greenland and record loss in 2019 detected by the GRACE-FO satellites. *Communications Earth & Environment*, *1*(8). https://doi.org/10.1038/s43247-020-0010-1

Schaeffer, A., & Lebedev, S. (2013). Global shear speed structure of the upper mantle and transition zone. *Geophysical Journal International*, *194*, 417–449. https://doi.org/10.1093/gji/ggt095

Simpson, M., Milne, G. A., Huybrechts, P., & Long, A. J. (2009). Calibrating a glaciological model of the Greenland ice sheet from the Last Glacial Maximum to present-day using field observations of relative sea level and ice extent. *Quaternary Science Reviews*, *28*, 1631–1657. https://doi.org/10.1016/j.quascirev.2009.03.004

Simpson, M., Wake, L., Milne, G. A., & Huybrechts, P. (2011). The influence of decadal- to millennial-scale ice mass changes on present-day vertical land motion in Greenland: Implications for the interpretation of GPS observations. *Journal of Geophysical Research*, *116*, B02406. https://doi.org/10.1029/2010jb007776

Steffen, R., Audet, P., & Lund, B. (2018). Weakened lithosphere beneath Greenland inferred from effective elastic thickness: A hotspot effect? *Geophysical Research Letters*, *45*(10), 4733–4742. https://doi.org/10.1029/2017gl076885

Tarasov, L., Dyke, A. S., Neal, R. M., & Peltier, W. R. (2012). A data-calibrated distribution of deglacial chronologies for the North American ice complex from glaciological modeling. *Earth and Planetary Science Letters*, *315*(316), 30–40. https://doi.org/10.1016/j.epsl.2011.09.010

Tarasov, L., & Peltier, W. (2002). Greenland glacial history and local geodynamic consequences. *Geophysical Journal International*, *150*, 198–229. https://doi.org/10.1046/j.1365-246x.2002.01702.x

The IMBIE Team. (2020). Mass balance of the Greenland Ice Sheet from 1992 to 2018. *Nature*, *579*, 233–239.

van Dam, T., Francis, O., Wahr, J., Khan, S. A., Bevis, M., & van den Broeke, M. R. (2017). Using GPS and absolute gravity observations to separate the effects of present-day and Pleistocene ice-mass changes in South East Greenland. *Earth and Planetary Science Letters*, *459*, 127–135. https://doi.org/10.1016/j.epsl.2016.11.014

Velicogna, I., Mohajerani, Y., Landerer, F., Mouginot, J., Noel, B., Rignot, E., et al. (2020). Continuity of ice sheet mass loss in Greenland and Antarctica from the GRACE and GRACE Follow-On missions. *Geophysical Research Letters*, *47*, e2020GL087291. https://doi.org/10.1029/2020gl087291

Wake, L., Lecavalier, B. S., & Bevis, M. (2016). Glacial Isostatic Adjustment (GIA) in Greenland: A review. *Current Climate Change Reports*, *2*, 101–111. https://doi.org/10.1007/s40641-016-0040-z

Watkins, M., Wiese, D. N., Yuan, D. N., Boening, C., & Landerer, F. W. (2015). Improved methods for observing Earth's time variable mass distribution with GRACE using spherical cap mascons. *Journal of Geophysical Research*, *120*, 2648–2671. https://doi.org/10.1002/2014jb011547

Woodroffe, S., Barlow, N., Wake, L., Kjeldsen, K., Bjork, A., Long, A., & Kjaer, K. (2017). *Saltmarsh record of post little ice age mass balance changes in Southeast Greenland*. AGU Fall Meeting. Abstract id C11B-0912.

Wouters, B., Gardner, A. S., & Moholdt, G. (2019). Global glacier mass loss during the GRACE satellite mission (2002–2016). *Frontiers of Earth Science*, *7*, 96. https://doi.org/10.3389/feart.2019.00096

Zhang, B., Liu, L., Khan, S. A., van Dam, T., Bjørk, A. A., Peings, Y., et al. (2019). Geodetic and model data reveal different spatio-temporal patterns of transient mass changes over Greenland from 2007 to 2017. *Earth and Planetary Science Letters*, *515*, 154–163. https://doi.org/10.1016/j.epsl.2019.03.028

Zhong, S., Paulson, A., & Wahr, J. (2003). Three-dimensional finite element modeling of Earth's viscoelastic deformation: Effects of lateral variations in lithospheric thickness. *Geophysical Journal International*, *155*, 679–695. https://doi.org/10.1046/j.1365-246x.2003.02084.x

Reference From the Supporting Information

Ivins, E., Watkins, M. M., Yuan, D.-N., Dietrich, R., Casassa, G., & Rülke, A. (2011). On-land ice loss and glacial isostatic adjustment at the Drake Passage: 2003–2009. *Journal of Geophysical Research*, *116*, B02403. https://doi.org/10.1029/2010jb007607